AGU PUBLICATIONS

JGR

Journal of Geophysical Research: Oceans

RESEARCH ARTICLE

10.1002/2015JC010810

Key Points:

- Empirical uncertainty functions for Arctic summer ice drift are formulated
- High-resolution SAR data are used to assess the uncertainty of Arctic ice drift
- Error assessment is conducted on Eulerian basis

Correspondence to:
H. Sumata,
hiroshi.sumata@awi.de

Citation:
Sumata, H., R. Kwok, R. Gerdes, F. Kauker, and M. Karcher (2015), Uncertainty of Arctic summer ice drift assessed by high-resolution SAR data, *J. Geophys. Res. Oceans*, *120*, 5285–5301, doi:10.1002/2015JC010810.

Received 2 MAR 2015
Accepted 10 JUN 2015
Accepted article online 12 JUN 2015
Published online 3 AUG 2015

Uncertainty of Arctic summer ice drift assessed by high-resolution SAR data

Hiroshi Sumata[1], Ronald Kwok[2], Rüdiger Gerdes[1,3], Frank Kauker[1,4], and Michael Karcher[1,4]

[1]Sea Ice Physics, Alfred Wegener Institute for Polar and Marine Research, Bremerhaven, Germany, [2]Jet Propulsion Laboratory, California Institute of Technology, California, USA, [3]Jacobs University, Bremen, Germany, [4]Ocean Atmosphere Systems, Hamburg, Germany

Abstract Time-space varying uncertainty maps of monthly mean Arctic summer ice drift are presented. To assess the error statistics of two low-resolution Eulerian ice drift products, we use high-resolution Lagrangian ice motion derived from synthetic aperture radar (SAR) imagery. The Lagrangian trajectories from the SAR data are converted to an Eulerian format to serve as reference for the error assessment of the Eulerian products. The statistical error associated with the conversion is suppressed to an acceptable level by applying a threshold for averaging. By using the SAR ice drift as a reference, we formulate the uncertainty of monthly mean ice drift as an empirical function of drift speed and ice concentration. The empirical functions are applied to derive uncertainty maps of Arctic ice drift fields. The estimated uncertainty maps reasonably capture an increase of uncertainty with the progress of summer melting season. The uncertainties range from 1.0 to 2.0 cm s^{-1}, which indicates that the low-resolution Eulerian products for summer seasons are of practical use for climate studies, model validation, and data assimilation, if their uncertainties are appropriately taken into account.

1. Introduction

One of the characteristics of the Arctic climate system is the existence of sea ice [*Wadhams*, 2002; *McPhee*, 2008]. Sea ice reflects the incoming solar radiation and hampers the direct exchange of heat, momentum, and materials between the atmosphere and ocean. These characteristics of sea ice are a distinctive feature of the atmosphere-ocean interaction in the polar oceans. To study dynamical and thermodynamical processes governing sea ice growth and retreat is therefore a topic of great interest to understand the ongoing dramatic change in the Arctic [e.g., *Comiso*, 2002; *Comiso et al.*, 2008; *Rampal et al.*, 2009; *Turner and Overland*, 2009; *Lindsay et al.*, 2009].

Sea ice motion deduced from satellite remote sensing offer valuable opportunities to study the dynamical processes governing the sea ice and its role in the Arctic climate system. In recent years, a number of sea ice motion products came to be available [e.g., *Kwok*, 2008; *Lavergne et al.*, 2010; *Girard-Ardhuin and Ezraty*, 2012; *Fowler et al*, 2013; *Kimura et al*, 2013]. These products provide ice displacements obtained by tracking spatial pattern of pixel intensities from one image at a certain time to another image at a subsequent time. By utilizing the displacement information, users can derive averaged ice drift vectors for a certain time interval. The inferred ice drift vectors are applied to a broad range of sea ice studies, e.g., sea ice dynamics [*Kimura and Wakatsuchi*, 2000; *Tremblay and Hakakian*, 2006; *Girard et al.*, 2009], the role of sea ice on the Arctic climate [*Spreen et al.*, 2009, 2011; *Kwok*, 2009; *Kwok et al.*, 2013], model validation [*Kreyscher et al.*, 2000; *Martin and Gerdes*, 2007; *Kwok et al.*, 2008; *Rozman et al.*, 2011], and data assimilation [*Meier et al.*, 2000; *Zhang et al.*, 2003; *Miller et al.*, 2006; *Stark et al.*, 2008; *Rollenhagen et al.*, 2009].

Sea ice motion data can be categorized into Eulerian and Lagrangian products. A number of products deduced from satellite-borne sensors are classified into Eulerian products, in which the initial locations of sea ice "parcels," representing a certain area at a certain time, are given at points on an equidistant gridded coordinate system, and ice movement of respective parcels after a certain time interval are given as ice displacements [e.g., *Kwok*, 2008; *Lavergne et al.*, 2010; *Girard-Ardhuin and Ezraty*, 2012; *Kimura et al.*, 2013; *Fowler et al.*, 2013]. The advantages of the Eulerian products are the uniform and extensive spatial and temporal coverage of data over the ice covered area and easiness of handling associated with the gridded feature in space and time. These advantages facilitate a variety of applications on the broad range of sea ice studies mentioned above. In particular, the uniform and extensive spatial and temporal coverages of the data are beneficial for Arctic-wide model validations and data assimilations.

Lagrangian products, on the other hand, give a sequential record of tracks (or trajectories) of distinctive ice parcels or identical spatial patterns of ice surface. There are two types of Lagrangian products available; one contains ice trajectories deduced from sequential records of positions of on-ice buoys [*Colony and Rigor*, 1989], while the other contains those deduced from high-resolution sequential images obtained from satellite-borne sensors (e.g., synthetic aperture radar (SAR)) [*Kwok*, 1998]. The advantages of the former types of the Lagrangian products are the higher accuracy of position measurements and robustness against misdetection of sea ice motion, while those for the latter products are the higher spatial density of coverage. In spite of the limited spatial and temporal coverages, the Lagrangian products are applied to a variety of sea ice studies [e.g., *Colony and Thorndike*, 1984; *Geiger et al*., 1998; *Kwok*, 2006; *Girard et al*., 2009].

For applications of the sea ice motion products, it is indispensable to appropriately evaluate the uncertainty of each ice drift vector. This requirement is rapidly growing due to the recent increase in the number of data assimilation studies using diverse data sets [e.g., *Nguyen et al*., 2011; *Sakov et al*., 2012; *Sumata et al*., 2013]. In systematic data assimilation, misfits between observed and modeled variables are quantified as a cost function (or an objective function), which is defined by the square of the norm of the difference divided by the corresponding uncertainties [e.g., *Menke*, 1989]. If more than one sort of physical variable are assimilated in a system, the relative importance of the different variables are evaluated based on their magnitude of uncertainties. Therefore uncertainty estimates for observed data are as important as data themselves.

However, in many Eulerian ice motion products uncertainty is not provided as a function of space and time, but rather as a constant value inferred from the study of comparison with Lagrangian buoy tracks [e.g., *Geiger et al*., 2000; *Lavergne et al*., 2010; *Hwang*, 2013]. This is because the number of available in situ measurements is still not sufficient to estimate the uncertainties Arctic wide and for the entire year. On the other hand, comparison studies of ice motion products [*Hwang and Lavergne*, 2010; *Rozman et al*., 2011; *Sumata et al*., 2014] imply that the difference of ice drift vectors between different products is not always consistent with the uncertainty provided for respective products. In addition, other studies pointed out that the error of ice drift is not spatially uniform [*Hwang*, 2013], but is covariant with sea ice properties such as ice concentration [*Kwok et al*., 1998] and/or ice drift speed [*Sumata et al*., 2014]. These studies, together with the requirement of data assimilation studies, demand the formulation of uncertainties as a function of space and time.

To tackle this issue, we formulate empirical uncertainty functions for Eulerian ice motions by means of utilization of Lagrangian products provided from the RADARSAT Geophysical Processor System (RGPS) [*Kwok*, 1998]. The RGPS provides high-resolution Lagrangian sea ice motions and other ice-related variables deduced from SAR imagery. We take advantage of the high spatial resolution of the RGPS data to assess the error statistics of low-resolution Eulerian products. Previous studies have used sparse buoy measurements for the assessment of the Eulerian products. Using the densely populated RGPS SAR data allows more thorough assessment of these products, e.g., it allows the definition of empirical uncertainty functions. Here, we convert the Lagrangian ice motion to Eulerian ice drift and use them as a reference for the assessment. As will be shown later, errors associated with the conversion can be decreased to an acceptable level by calculating spatial and temporal averages of the Lagrangian ice motions to derive monthly mean Eulerian drift. The temporal averaging is an indispensable procedure because of the irregular sampling time intervals of the Lagrangian product. Since previous studies pointed out that the error of the Eulerian products is covariant with ice concentration [*Kwok et al*., 1998] and ice drift speed [*Sumata et al*., 2014], we examine the error statistics of Eulerian products in relation to ice concentration and ice drift speed.

To demonstrate uncertainty estimation for Eulerian products, we formulate empirical error functions for monthly mean ice drift in summer season (May–July). The summer ice drift data with appropriate uncertainty estimates are essential for ongoing model validation and data assimilation studies. Recent reduction of summer sea ice extent and ice concentration in the Arctic highlights the necessity of validation of modeled dynamical processes under fragile ice conditions [*Rampal et al*., 2011]. Since models struggle to reproduce realistic Arctic sea ice properties in summer, data assimilation schemes need summer ice drift and associated uncertainties to constrain these models, and to validate (calibrate) dynamical processes under fragile ice condition. Providing time-space varying uncertainty maps for monthly mean ice drift is beneficial for a wide range of studies, since monthly mean drift has been used to a variety of studies because of its ease of handling [e.g., climate studies: *Wu et al*., 2006; *Wang and Zhao*, 2012, model validation: *Martin and Gerdes*, 2007, and model's parameter estimation: *Miller et al*., 2006; *Nguyen et al*., 2011; *Sumata et al*., 2013].

We selected two Eulerian ice motion products, which provides ice motions not only in winter but also in summer. The selected products are Polar Pathfinder Daily 25 km EASE-Grid Sea Ice Motion Vectors, Version 2 (hereafter NSIDC2) [*Tschudi et al*., 2010; *Fowler et al*., 2013] from the National Snow and Ice Data Center (NSIDC) and ice drift vectors from *Kimura et al*. [2013] (hereafter KIMURA) at University of Tokyo. Although other providers also published Eulerian sea ice motion in summer (e.g., sea ice motion from *Kwok* [2008], Ocean and Sea Ice Satellite Application Facility (OSISAF); *Lavergne et al*. [2010]), we focus our attention on the aforementioned products because only those are available over the same time period as the RGPS data product.

The paper is organized as follows: section 2 describes the data products, section 3 describes the derivation of Eulerian ice drift from the RGPS Lagrangian trajectory, section 4 describes the formulation of uncertainties for the Eulerian products, and finally section 5 gives concluding remarks.

2. Data

2.1. RGPS Lagrangian Ice Motion Product

To assess the error of the low-resolution Eulerian ice motion products, we utilize the high-resolution Lagrangian ice motion product provided from RGPS [*Kwok*, 1998] as a reference. RGPS is developed and maintained at the Jet Propulsion Laboratory (JPL) and provides different types of sea ice products obtained from RADARSAT SAR imagery [*Kwok et al*., 2000; *Kwok and Cunningham*, 2014]. Taking advantage of its high-resolution feature, the data have been applied to a number of studies which require fine-scale information of sea ice motion and deformation [e.g., *Kwok*, 2002, 2006; *Kwok and Cunningham*, 2002; *Lindsay*, 2002; *Stern and Moritz*, 2002]. The Lagrangian ice motion product is obtained by tracking spatial pattern of pixels in sequential images with the maximum correlation technique [*Fily and Rothrock*, 1987; *Kwok et al*., 1990]. The spatial resolution (i.e., the spatial separation of the initial seeds of traced ice parcels) is approximately 10 km and the temporal resolution of the acquired imagery ranges from 1.5 h to 15 days (The sampling is irregular in time; the bulk interval is approximately 3 days). The RGPS record provides ice motion from 1996 to 2008, although no data are available in September and October for the entire period, and only partially available in August and November. There are additional unavailable months in 1996, 1997, 2000, 2002, and 2008. The data are provided on a polar stereographic grid, the reference latitude of which is 70°N, and the origin of the Cartesian grid is at the North Pole. The error statistics of the Lagrangian motion were closely examined in *Lindsay and Stern* [2003] by the comparison of the tracks from different facilities and the comparison with buoy trajectories from the International Arctic Buoy Program [*Colony and Rigor*, 1989]. The paper reported that the error standard deviation of the tracking associated with manual interventions is 100 m, and the magnitude of the displacement difference relative to the buoy data is 323 m.

The data set is assembled as monthly collections of data files. Each monthly collection contains several data files, each gives a set of trajectories of ice parcels obtained from a certain data stream. In each data stream, the initial locations of ice parcels are defined on the image frame of an initial data-take and the respective parcels are tracked in sequential images to provide trajectories. Each trajectory in each data stream is composed of a sequential record of observations, in which the time, location, a quality flag, and other information are given. In the present application, we utilize all trajectory data, which contain at least one observation for summer months (May–August) from 1997 to 2008.

2.2. NSIDC Eulerian Ice Motion Product

NSIDC provides one of the most comprehensive set of Eulerian ice motion products for the Arctic Ocean, Polar Pathfinder Daily 25 km EASE-Grid Sea Ice Motion vectors, Version 2 [*Tschudi et al*., 2010; *Fowler et al*., 2013], which currently extends from 1978 to 2012 and covers the entire Arctic Ocean for all seasons (Hereafter referred to as NSIDC2). The product contains daily gridded fields of sea ice. The product has been widely used in modeling and data assimilation studies [e.g., *Miller at al*., 2006; *Dai et al*., 2006; *Stark et al*., 2008]. The used algorithm calculates sea ice motion using a variety of satellite-based sensors (Advanced Very High-Resolution Radiometer (AVHRR), Scanning Multichannel Microwave Radiometer (SMMR), Special Sensor Microwave Imager (SSM/I), and Advanced Microwave Scanning Radiometer for EOS (AMSR-E)), as well as the International Arctic Buoy Program (IABP) observations and wind effects on ice motion [*Thorndike and Colony*, 1982]. All passive microwave sensors are used during their time of operation (SMMR until 1987, AMSR-E 2002–2011, SSM/I 1987–2012), and AVHRR use drops after 2006, because of its limited coverage due to cloud cover/contamination. Recent (post-2011) sea ice motions are therefore obtained from SSM/I, IABP buoys, and wind forcing, but the full data set retains the integration of other sensors during the aforementioned time periods. NCEP Reanalysis wind data [*Kalnay et al*., 1996] are used for the entire data set. Sea ice motions are obtained from each satellite sensor using the Maximum Cross Correlation (MCC) method and merged with the buoy data and winds using the cokriging method described in *Isaak and Srivastava* [1989]. The sea ice motion vectors are defined on an EASE-Grid with 25 km $\times$ 25 km horizontal resolution on a daily basis. We define monthly mean drift on an Eulerian grid described in section 3, if the temporal coverage of the daily motion vectors of the corresponding month is 100%. The monthly mean drift vectors for seven summer seasons (May–July) are used to formulate an error function.

2.3. KIMURA Eulerian Ice Motion Product

We also consider ice drift data from *Kimura et al*. [2013], which provides ice drift not only in winter, but also in summer (Hereafter referred to as KIMURA; In *Kimura et al*. [2013] only winter data are described, but summer data are also provided based on the same method). The winter ice drift (December–April) is calculated from brightness temperature maps of AMSR-E 89 GHz horizontal and vertical polarization channels, whereas the summer drift (May–November) is obtained from 18.7 GHz channels. The algorithm used to detect ice motions is the improved MCC method described in *Kimura and Wakatsuchi* [2000, 2004]. The nominal time interval of consecutive images used to detect ice displacement is 24 h. In order to provide ice drift over the entire ice covered area, they filled missing values by an average of surrounding values, if more than 5 of the surrounding 8 points give an appropriate ice drift. They repeated this procedure twice for the product. The data cover the Arctic Ocean with a horizontal resolution of 37.5 km $\times$ 37.5 km in winter and with a resolution of 75 km $\times$ 75 km in summer. The data are currently available from September 2002 to April 2011. The monthly mean drift is defined on the Eulerian grid coordinate in the same manner as NSIDC2 with a maximum interpolation distance of 53 km. For the present error formulation, we apply the monthly mean ice drift vectors from five summer seasons (May–July).

2.4. OSISAF Ice Concentration Product

In order to formulate the uncertainty of ice drift as a function of ice concentration, we use ice concentration data provided from OSISAF. For the data period used in this study (1997–2007), the raw data are measured by SSM/I and are processed following the algorithms described in *Eastwood et al*. [2010]. Here, we utilize the product named OSI-409, which contains daily mean ice concentration on a polar stereographic grid with a horizontal spacing of 10 km, covering the entire Arctic Ocean. We processed the original OSI-409 data into monthly mean data on the Eulerian grid. In this process only data whose status flags guarantee their reliability are used. Monthly mean values are defined at a grid point if more than 80% of the days of the month have reliable data. For the data projection from the Polar-Stereographic grid to the Eulerian grid, we simply calculated the arithmetical mean of valid data contained in each Eulerian grid cell. In general, each grid cell contains a sufficiently large number of data points because of the finer resolution of the ice concentration data, leading to a negligible interpolation error.

3. Derivation of Eulerian Ice Drift for Reference

We process the RGPS Lagrangian trajectory data into monthly mean Eulerian ice drift vectors. First we define "Lagrangian" ice drift vectors from all pairs of sequential record of observations contained in the trajectory data, except for the pairs whose time difference is smaller than 1 day or larger than 10 days. A Lagrangian vector gives an averaged displacement of an ice parcel from a certain position to another position for a certain time interval, and has information regarding the initial and the terminal positions and corresponding time span.

Second we define monthly mean Eulerian ice drift vectors. The Eulerian coordinate system for the vector is formulated on a spherical rotated grid of the Earth, whose geographical north pole is shifted to 60°E on the equator. The coordinate system offers nearly equidistant grid cells in the Arctic Ocean, whose horizontal resolution is 54.8 km $\times$ 54.8 km. The Eulerian ice drift at each grid point is defined by an average of all Lagrangian vectors whose initial or terminal position lies within the distance R from the center of each grid

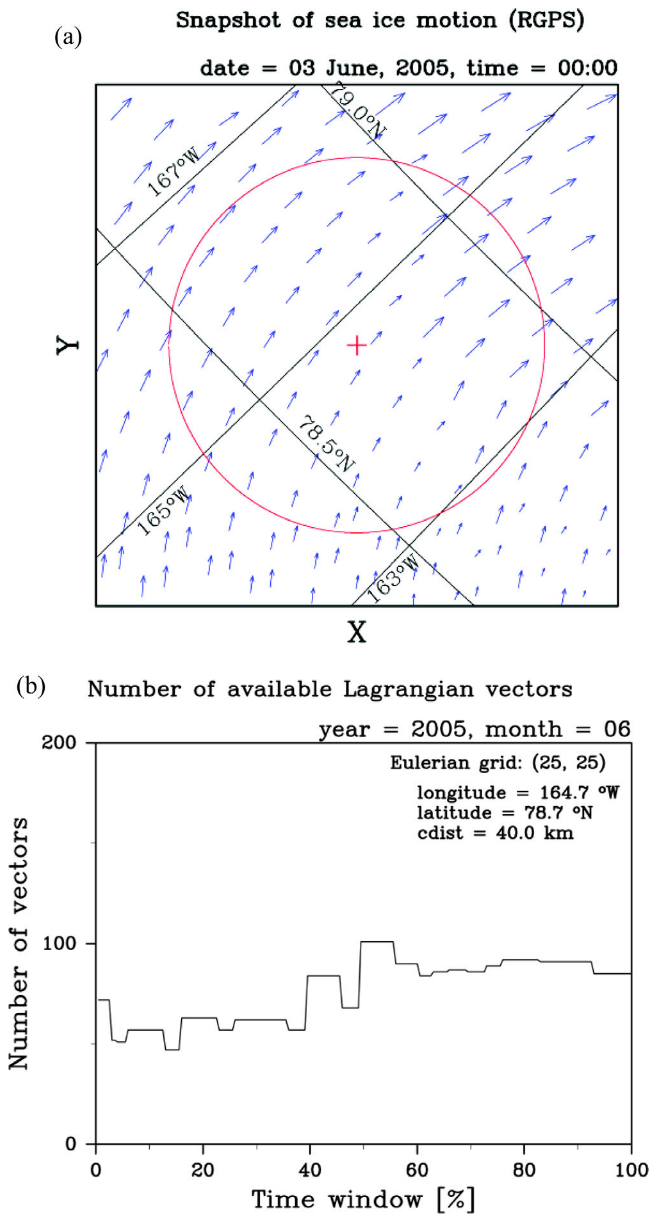

Figure 1. (a) Lagrangian sea ice drift vectors (blue arrow) around an Eulerian grid point (red plus; 164.7°W, 78.7°N) on 3 July 2005, and (b) the time series of the number of available Lagrangian vectors for monthly mean calculation at the Eulerian grid point. In Figure 1a, only the Lagrangian drift vectors whose time span intersects 0:00 on 3 July 2005 are shown by motion vectors. Note that each Lagrangian vector exhibits an averaged track of "ice parcel" from its initial location to the terminal location during its time span, i.e., the magnitude of the vector does not correspond to sea ice drift speed, since the time span of each vector differs each other. The red circle in Figure 1a indicates the area used to calculate averaged Eulerian drift vector. Figure 1b exhibits number of Lagrangian vectors contained in the red circle at each time segment, corresponding to $g(\boldsymbol{x}, t)$ in equation (1). See text for description.

point (R = 40.0 km, which corresponds to the half distance between diagonally neighboring Eulerian grid points), and whose initial or terminal times lies in the corresponding month. Figure 1a shows an example of a grid point (red plus) and area for the averaging (red circle), with Lagrangian vectors (blue arrows) whose time span intersects 0:00 on 3 June, 2005. Note that the number of available Lagrangian vectors is different for each Eulerian grid point and is not constant in time. Figure 1b shows the number of available Lagrangian vectors for the monthly mean at the grid point shown in Figure 1a.

In order to guarantee equal contributions from each time segment on the temporal mean, we take temporal weighting into account to define the monthly mean;

$$\vec{v_E}\,(\boldsymbol{x}) = \sum_{i=1}^{N(\boldsymbol{x})} \frac{1}{T} \int_{T_1(i)}^{T_2(i)} \frac{\vec{v_L}(\boldsymbol{x}, i)}{g(\boldsymbol{x}, t)} dt, \qquad (1)$$

where $\vec{v_E}$ is a monthly mean Eulerian ice drift vector at position $\boldsymbol{x}$, $\boldsymbol{x}$ is a location on the Eulerian grid coordinate, $N(\boldsymbol{x})$ is the number of available Lagrangian ice drift vectors for the monthly mean at location $\boldsymbol{x}$, T is a time interval to define the monthly mean (30 or 31 days), $T_1(i)$ and $T_2(i)$ are the initial and the terminal time defining the i-th Lagrangian drift vector, $\vec{v_L}(\boldsymbol{x}, i)$ is the i-th Lagrangian vector available for the monthly mean calculation at location $\boldsymbol{x}$, and $g(\boldsymbol{x}, t)$ is the number of available Lagrangian vectors at a certain time segment Δt for the mean calculation at $\boldsymbol{x}$. To define monthly mean Eulerian vectors on the gridded coordinate, we beforehand calculate $g(\boldsymbol{x}, t)$ at all monthly mean grid points. If no Lagrangian vector is available at any time segment of the month at $\boldsymbol{x}$ (i.e., $g(\boldsymbol{x}, t) = 0$), the monthly mean at that point is not defined. The temporal coverage in August does not allow to calculate monthly mean Eulerian vectors.

To estimate the error associated with the derivation of the Eulerian vectors, we examine the distribution function of the difference between an estimated Eulerian vector and the Lagrangian vectors used to define the Eulerian vector (Figure 2). The functions were obtained from the combinations of the all Eulerian and corresponding Lagrangian vectors. The figure shows that the form of the probability density functions

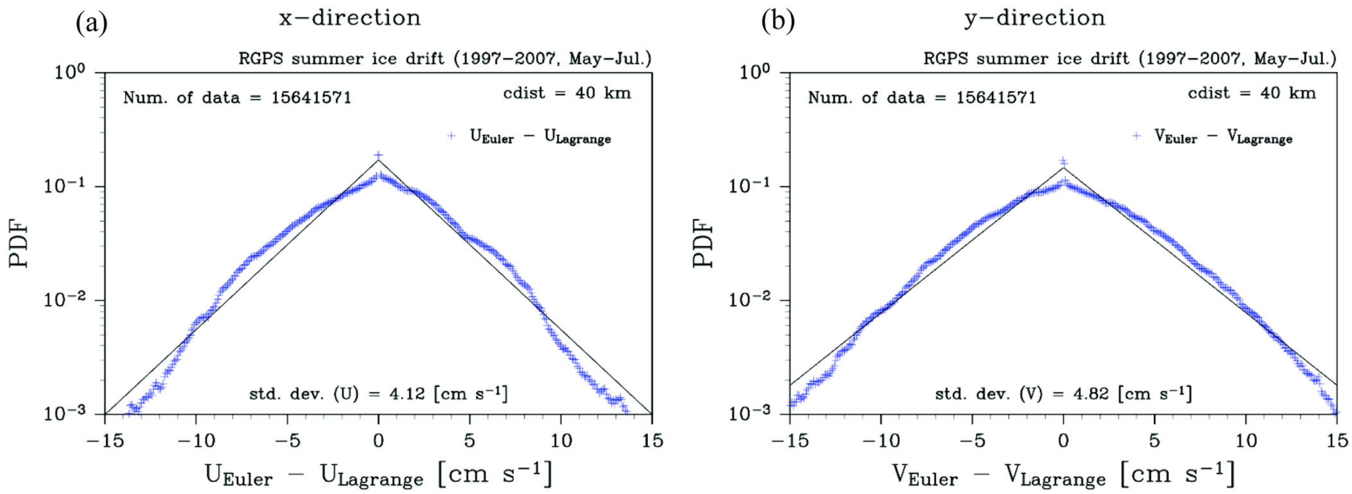

Figure 2. Probability density functions of difference between monthly mean Eulerian ice drift and raw Lagrangian ice drift used to calculate the monthly mean in (a) *x* and (b) *y* direction. The solid black line in each plot depicts corresponding Laplace distribution. The functions are obtained from RGPS summer ice drift (May–July) from 1997 to 2007. See text for description.

(PDFs) can be reasonably well approximated by the Laplace (the double exponential) distribution (black line in Figure 2);

$$\mathcal{Q}\left(u_E-u_L\right)=\frac{1}{2b}\exp\left(-\frac{|u_E-u_L|}{b}\right), \tag{2}$$

whose variance is given by

$$2b^2=\left(\sum_{j=1}^{M}N(j)-1\right)^{-1}\sum_{j=1}^{M}\sum_{i=1}^{N(j)}\left(u_E(j)-u_L(i,j)\right)^2, \tag{3}$$

where M is the total number of the estimated Eulerian vectors, $N(j)$ is the number of the Lagrangian vectors used to define the j-th Eulerian vector, $u_E(j)$ is the zonal (x) component of the j-th Eulerian vector, and $u_L(i,j)$ is also the zonal (x) component of the i-th Lagrangian vector used to define the j-th Eulerian vector. Since the functional form of the distribution is obtained from a sufficiently large number of samples $O(10^7)$, we regard the function as the one which describes the population. If we deal with each Lagrangian vector as an independent stochastic variable whose probability density function is given by (2), the standard deviation of the mean (i.e., the standard error of an estimated Eulerian vector) with N samples is given by $\sqrt{2}bN^{-\frac{1}{2}}$.

We used a threshold of $N=400$ to define the Eulerian vectors. This gives standard errors of the x and y component of the Eulerian vectors of 0.21 and 0.24 cm s^{-1}, respectively, which is, as will be shown in later, one order of magnitude smaller than the errors of the low-resolution Eulerian products. At the same time the calculation of the monthly mean with this threshold reduces the error involved in the Lagrangian vectors on the monthly mean. If we estimate the uncertainty associated with the manual intervention and the geolocation error on each Lagrangian drift by 0.16 cm s^{-1} (i.e., the manual intervention error 100 m plus the geolocation error 323 m divided by the bulk time interval 3 days), the associated error of the monthly mean Eulerian vector is 8×10^{-3} cm s^{-1} (0.16 cm s^{-1} / $N^{1/2}$). This error is more than two orders of magnitude smaller than the error of the Eulerian products.

Figure 3a shows the number of Lagrangian vectors available for the monthly mean calculation in June 2005. The RGPS Lagrangian product offers a sufficiently large number of vectors allowing a strict threshold of $N=400$. Figure 3b depicts the Eulerian vector field for the same time. The estimated Eulerian vectors are used as reference data to examine error statistics of the low-resolution Eulerian products. It should be noted here that Figures 1 and 3 are selected to demonstrate the derivation of the Eulerian vectors from the densely populated RGPS Lagrangian motions, and are not representing a typical situation. From the point of view of spatial and temporal coverage, June 2005 is one of the "champion months." Since we can derive

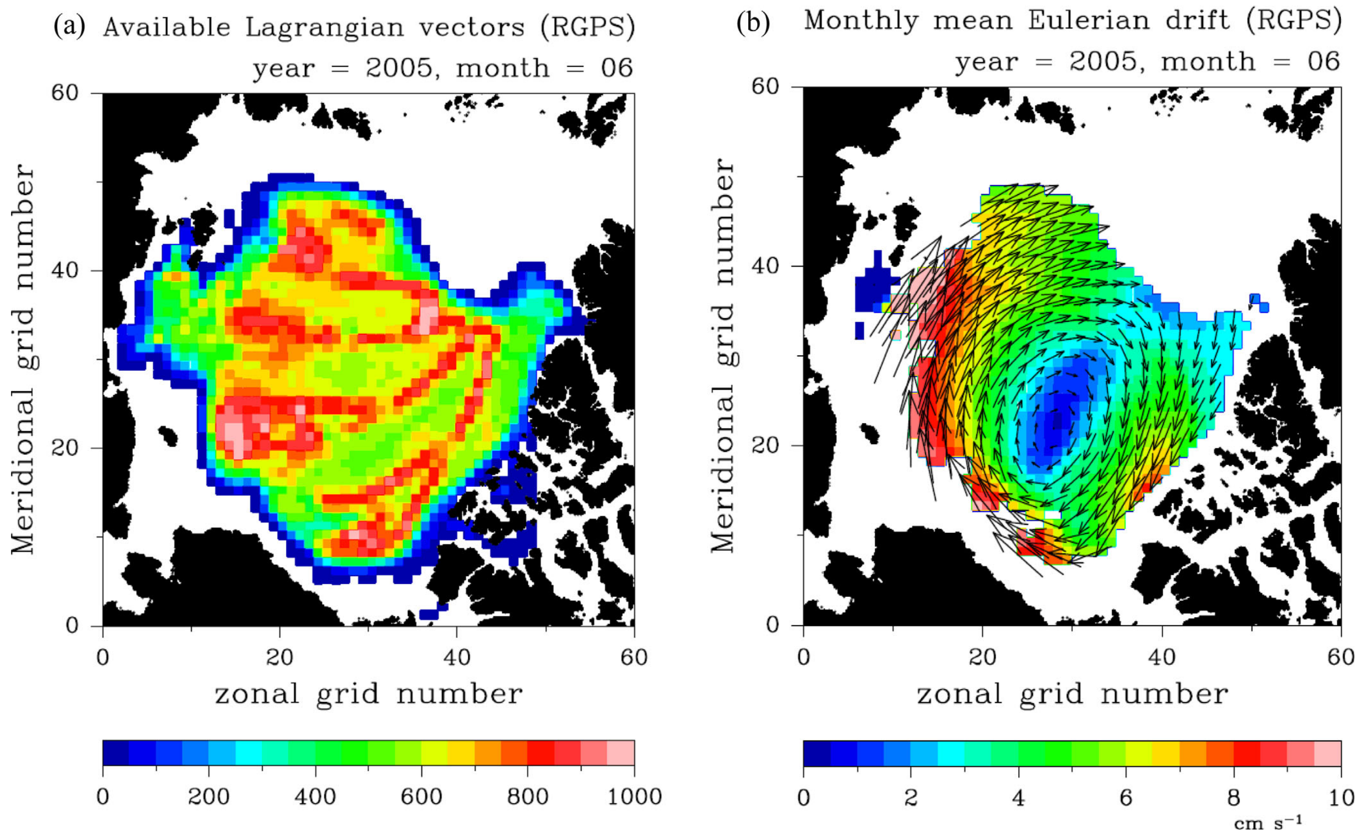

Figure 3. Spatial distribution of (a) number of available RGPS Lagrangian vectors for the monthly mean calculation in June 2005 and (b) deduced corresponding monthly mean Eulerian ice drift with a threshold of 400 Lagrangian vectors. Only every second vector is shown in *x* and *y* direction.

monthly mean Eulerian vectors in only limited areas in some months, the statistical examinations of the following section are only possible by combining the RGPS data for the entire period of operation.

4. Uncertainty Formulation

Figure 4 shows an example of the spatial pattern of the monthly mean ice drift in June 2005 from NSIDC2 and KIMURA (See also Figure 3b for RGPS in the same month). The figure exhibits typical features of the respective products. NSIDC2 generally gives a smooth spatial pattern consistent with RGPS, whereas the magnitude of the ice drift vectors is smaller than that of RGPS in regions where RGPS gives large drift speed ($>$ 6 cm s^{-1}). KIMURA gives comparable drift speed with RGPS in such areas, whereas the direction of the ice drift vector exhibits small scale variation and the spatial pattern is noisier than that of RGPS. Note that the area showing large difference between the two products is close to the outer rim of the pack ice and relatively low ice concentration area ($\sim$90%). The spatial coverages of the both products are generally much larger than that of RGPS. We use ice drift vectors from the respective products for the respective uncertainty formulation, if both RGPS and the product provide ice drift at a certain grid point.

To formulate uncertainties for the selected products, first we examine the relation between the error of the respective products and ice drift speed, and second we examine the relation between the error and ice concentration. In both examinations, the "error" of the respective ice drifts are measured by the deviation from the corresponding RGPS monthly mean ice drifts, and therefore inevitably contains uncertainty coming from RGPS drift as described in section 3. It should be noted here that in the present uncertainty formulation we measure the error by the magnitude of the difference of two vectors, i.e., $||\vec{U}_{diff}||=||\vec{U}_{RGPS}-\vec{U}_{product}||$, where $||\vec{A}||$ is the magnitude (norm) of a vector $\vec{A}$(see Figure 5a). This definition does not directly measure the difference of ice drift speed, $||\vec{U}_{RGPS}||-||\vec{U}_{product}||$, nor the difference of drift direction, $\cos^{-1}[(\vec{U}_{RGPS}\cdot\vec{U}_{product})(||\vec{U}_{RGPS}||\,||\vec{U}_{product}||)^{-1}]$, but implicitly measures both of them. Advantages of the

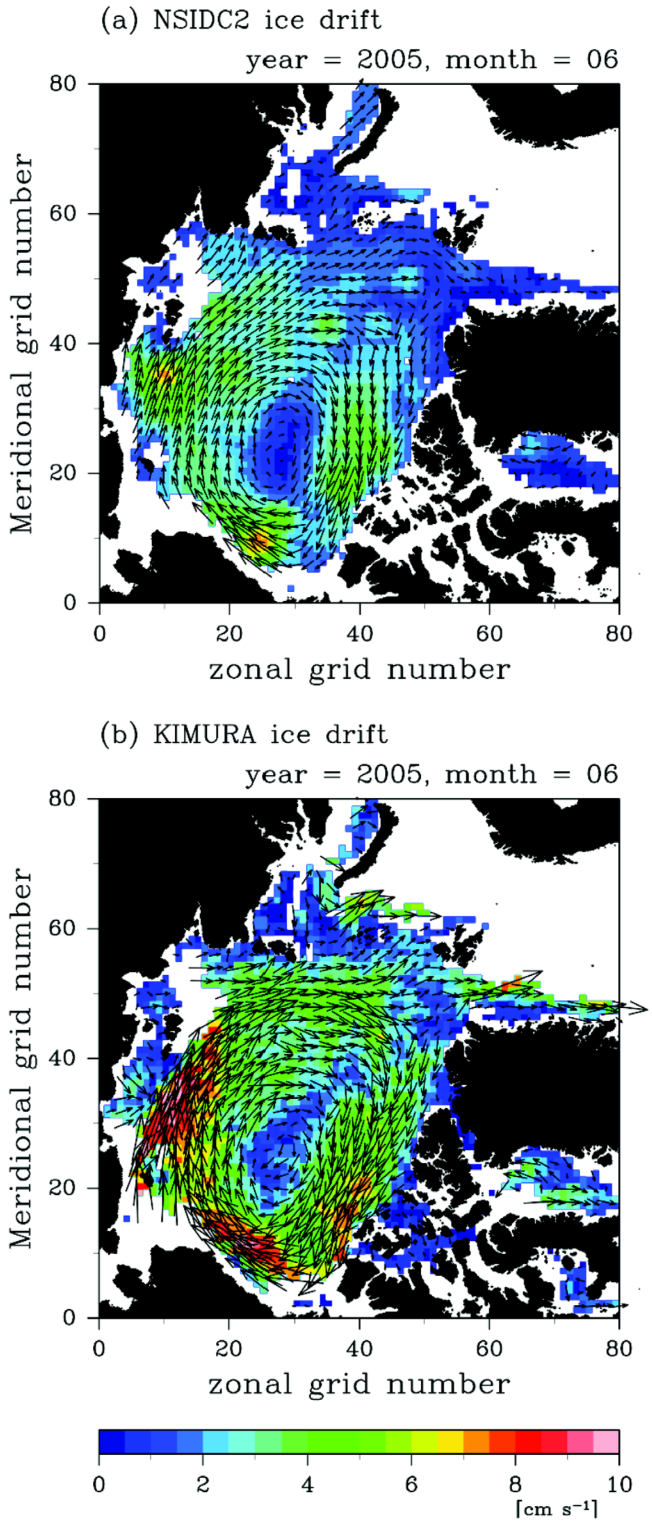

Figure 4. Monthly mean ice drift of (a) NSIDC2 and (b) KIMURA in June 2005. The color indicates ice drift speed.

present measure are (1) the uncertainties can be quantified by one scalar variable, $||\vec{U}_{diff}||$, (2) we do not need to assume an anisotropy of the uncertainty, and (3) estimated uncertainties can be directly applied to a different coordinate system without vector rotation. The practical usage of the estimated uncertainty function will be discussed in section 5.

Figure 6 shows scatter plots of the ice drift error (deviation from RGPS) against ice drift speed of both products. In Figure 6a, we can see that the error is not uniformly distributed but is dependent on the ice drift speed (the dense range of the points for 0–2 cm s^{-1} ice drift speed (abscissa) is approximately 0.2–3.0 cm s^{-1} range (ordinate), whereas that for 2–4 cm s^{-1} speed is approximately 0.4–6 cm s^{-1} range). This indicates that the distribution function of the error may differ in different ice drift speed ranges and should be formulated as a function of ice drift speed.

To take the possible difference of the functional forms into account, we classify the scatter points into six drift speed bins, i.e., five bins with 1 cm s^{-1} interval from 0 to 5 cm s^{-1} and a bin with drift speed larger than 5 cm s^{-1}. Figure 7a is an example of the distribution function of the error for 4–5 cm s^{-1} bin for NSIDC2. The figure shows that the distribution can be reasonably approximated by the lognormal function shown in the black line in the figure;

$$f\left(||\vec{U}_{diff}||\right)=\frac{1}{\sqrt{2\pi}\sigma_k||\vec{U}_{diff}||}\exp\left[-\frac{\left(\ln||\vec{U}_{diff}||-\mu_k\right)^2}{2\sigma_k^2}\right], \tag{4}$$

where σ_k and μ_k are distribution parameters calculated from the distribution of the points in the k-th bin. We examined functional forms of the points in all bins and found that in all bins the distributions can be reasonably approximated by lognormal functions with the distribution parameters obtained from the points in the corresponding bins (see Appendix A). From the lognormal function in each bin, we can define the cumulative distribution function in k-th bin as

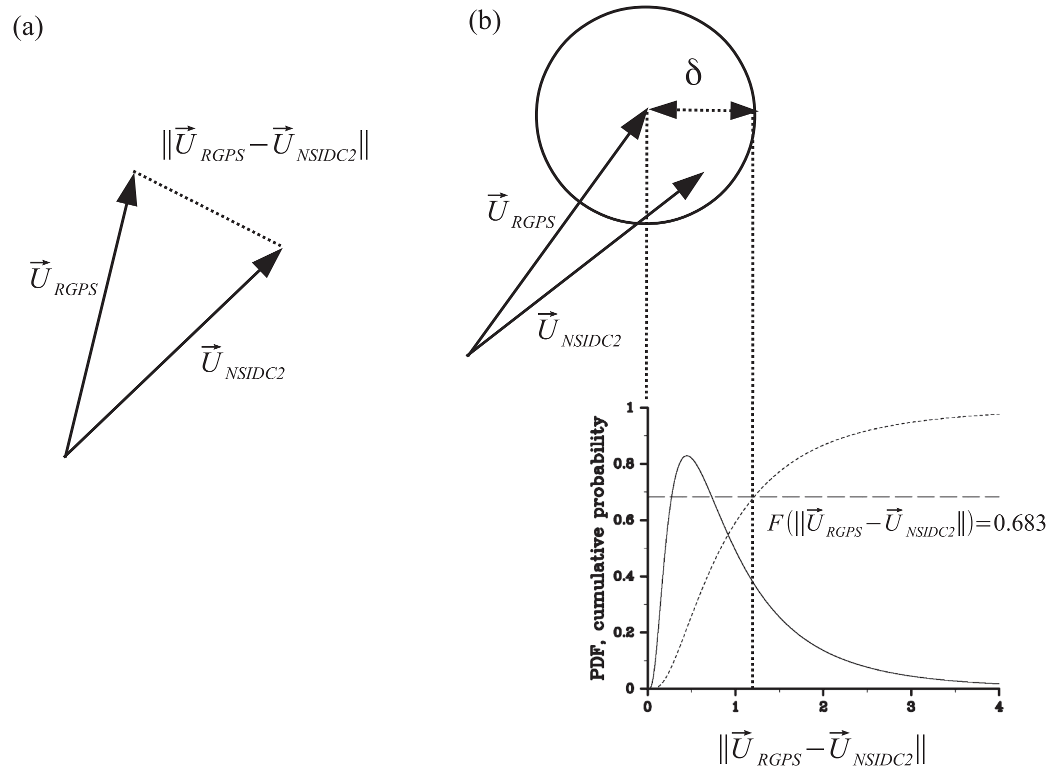

Figure 5. Sketch of (a) the magnitude of ice drift difference between NSIDC2 and RGPS and (b) the definition of ice drift uncertainty as the 68.3 percentile of the cumulative function, *F*. See text for description.

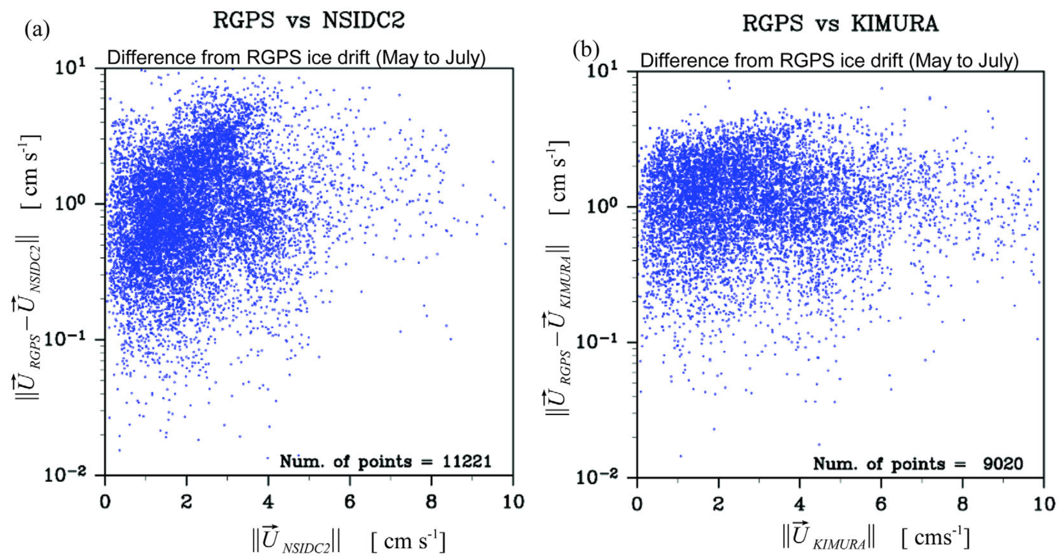

Figure 6. Scatter plot between the monthly mean ice drift speed (a: NSIDC2, b: KIMURA) and the magnitude of their difference from the monthly mean RGPS ice drift.

$$F\left(||\vec{U}_{diff}||\right)=\frac{1}{2}\mathrm{erfc}\left[-\frac{\ln||\vec{U}_{diff}||-\mu_k}{\sqrt{2}\sigma_k}\right], \tag{5}$$

where $\mathrm{erfc}(x)=2\pi^{-1/2}\int_x^\infty \exp[-t^2]dt$ is the complementary error function (see Figure 7b).

In the present uncertainty formulation, we measure the uncertainty of the ice drift vectors, $\delta_{||\vec{U}||}$, by the 68.3 percentile of the cumulative distribution function of each bin (the subscript of δ indicates that the error is a

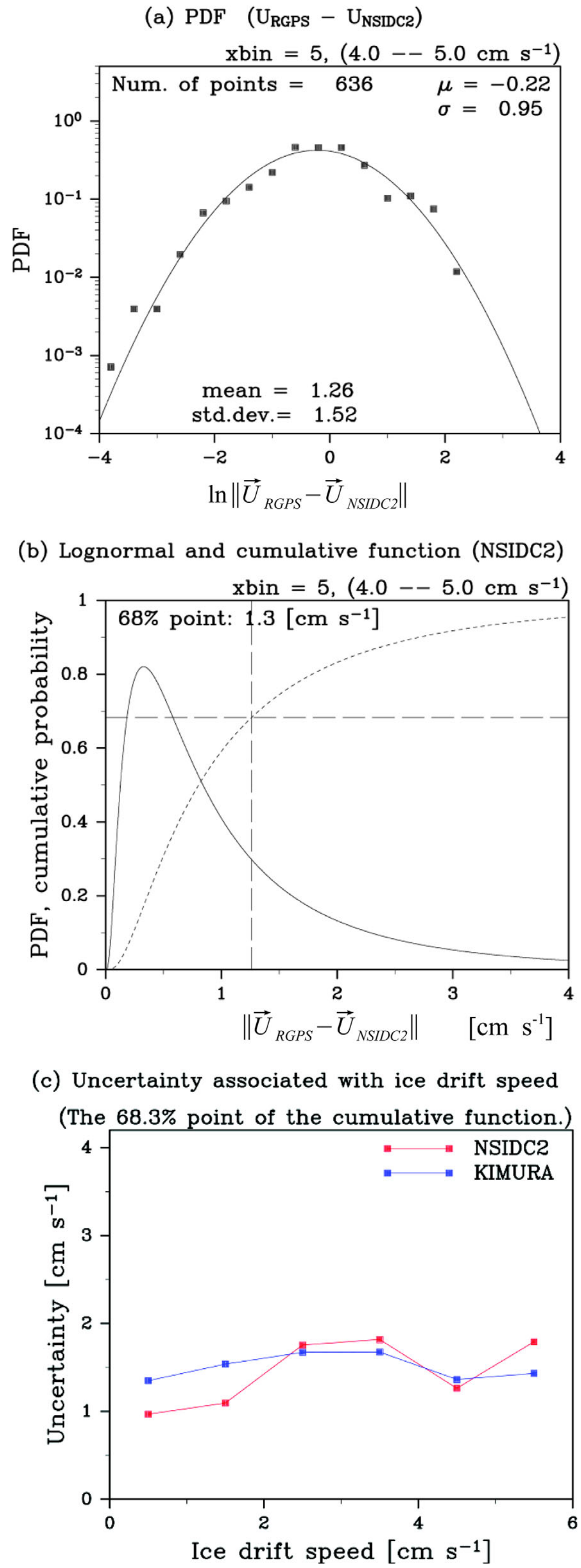

Figure 7. (a) Probability density function (PDF) of ice drift difference between NSIDC2 and RGPS in 4.0–5.0 cm s^{-1} ice drift speed bin, (b) PDF of the corresponding lognormal function (solid line) and its cumulative function (dotted line) in the same bin, and (c) estimated ice drift uncertainty as a function of ice drift speed for NSIDC2 (red) and for KIMURA (blue). The solid line in Figure 7a exhibits a lognormal distribution whose distribution parameters are obtained from the ice drift difference in the corresponding bin. The horizontal and vertical dashed lines in Figure 7b indicates 68.3 percentile of the cumulative function (horizontal) and its corresponding value of ice drift difference. See text for description.

function of ice drift speed). This measure supposes that the error (magnitude of the difference from the referencing RGPS vector) is governed by a stochastic process, where the PDF is given by (4). The physical meaning of this measure is that the probability of the error being contained within a circle of the radius $\delta_{||\vec{U}||}$ is 68.3% (see Figure 5b). This measure corresponds to the error definition of the one-standard deviation for a random variable with a Gaussian distribution. Note that the present definition is not the same as the one employed in *Sumata et al*. [2014]. In their study uncertainty of a variable with lognormal distribution is measured by a combination of the mean and standard deviation of the distribution (which generally gives larger error than the present definition). Since we intend to provide uncertainty estimates applicable to the data assimilation of data from multiple sources, an error definition which can be easily relatable to that of Gaussian distribution is preferable (see also discussion in section 5).

The estimated uncertainties for the respective drift speed bins are summarized in Figure 7c. The uncertainty of NSIDC2 ranges from 1.0 to 1.8 cm s^{-1}, while that of KIMURA ranges from 1.3 to 1.7 cm s^{-1}. In the low-speed range, NSIDC2 gives smaller uncertainty associated with the smooth and aligned ice drift vectors, whereas a clear low speed bias of NSIDC2 [*Sumata et al*., 2014] increases error in the middle and high-speed ranges. The uncertainty of KIMURA does not exhibit clear dependence on drift speed, whereas it gives relatively large uncertainty even in the low-speed range due to the noisy spatial pattern (Figure 4b).

Next we formulate uncertainties associated with ice concentration. We examine relations between ice drift error and ice concentration in the same approach as for ice drift speed (Figure 8). The scatter of the points

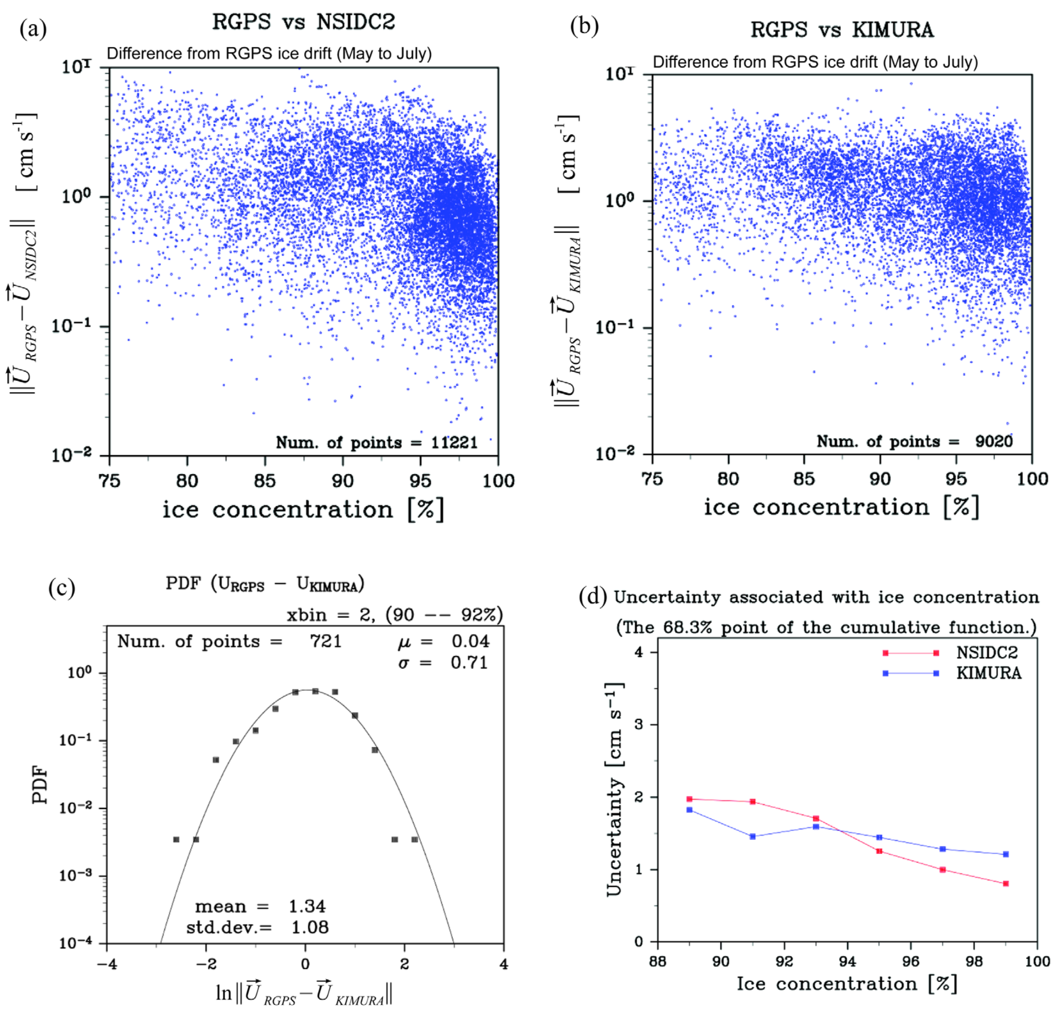

Figure 8. (a) and (b) Scatter plot between the monthly mean ice concentration and difference of the monthly mean ice drift (a: NSIDC2, b: KIMURA) from the RGPS ice drift. Figure 8c shows an example of PDF of ice drift difference between KIMURA and RGPS in 90–92% ice concentration bin. (d) Estimated ice drift uncertainty as a function of ice concentration for NSIDC2 (red) and for KIMURA (blue). See text for description.

shown in Figures 8a and 8b again classified into six different ice concentration bins, i.e., an ice concentration bin lower than 90% and five bins from 90% to 100% with 2% interval. We examined the functional form of the PDF in each bin and found that the distribution in all bins are again well represented by lognormal functions with corresponding distribution parameters (not shown all, see Figure 8c for an example);

$$h\left(||\vec{U}_{diff}||\right)=\frac{1}{\sqrt{2\pi}\sigma_l||\vec{U}_{diff}||}\exp\left[-\frac{\left(\ln||\vec{U}_{diff}||-\mu_l\right)^2}{2\sigma_l^2}\right], \tag{6}$$

where σ_l and μ_l are the distribution parameters in l-th ice concentration bin calculated from the distribution of the points in the bin. The cumulative distribution function for l-th bin is

$$H\left(||\vec{U}_{diff}||\right)=\frac{1}{2}\mathrm{erfc}\left[-\frac{\ln||\vec{U}_{diff}||-\mu_l}{\sqrt{2}\sigma_l}\right]. \tag{7}$$

Figure 8d summarizes the uncertainties defined by the 68.3 percentile of the cumulative distribution function (7). The uncertainties of the both products exhibit a clear tendency toward larger uncertainties in the low ice concentration ranges and smaller uncertainties in the high ice concentration ranges. Since the tendency is more emphasized in NSIDC2, KIMURA gives relatively smaller uncertainty in the low ice concentration area, whereas NSIDC2 gives smaller uncertainty in the high ice concentration area.

We define the total uncertainty ϵ as a combination of the uncertainty associated with ice drift speed and that associated with ice concentration,

$$\epsilon\left(||\vec{U}||,a\right)=\mathrm{Max}\left(\delta_{||\vec{U}||},\delta_a\right), \tag{8}$$

where $\delta_{||\vec{U}||}$ and δ_a are uncertainties associated with ice drift speed and ice concentration, defined by the 68.3 percentile of the cumulative distribution functions (5) and (7), respectively. Figure 9 shows the functional form of (8) in a two-dimensional view. The empirical uncertainty function (8) for both products exhibits larger uncertainty values at low ice concentration and high-uncertainty plateau at 2–4 cm s^{-1} drift speed

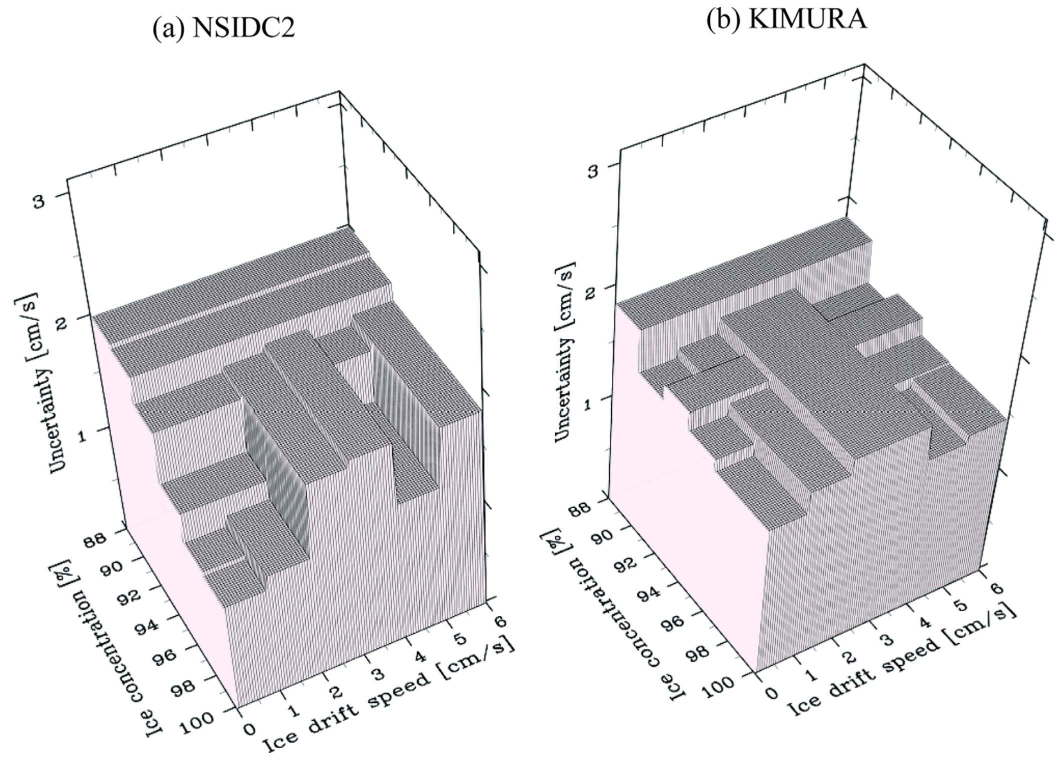

Figure 9. Estimated uncertainty of ice drift (a) NSIDC2 and (b) KIMURA, as a function of ice drift speed and ice concentration. The uncertainty is given by 6 × 6 segment of ice drift speed and ice concentration bins.

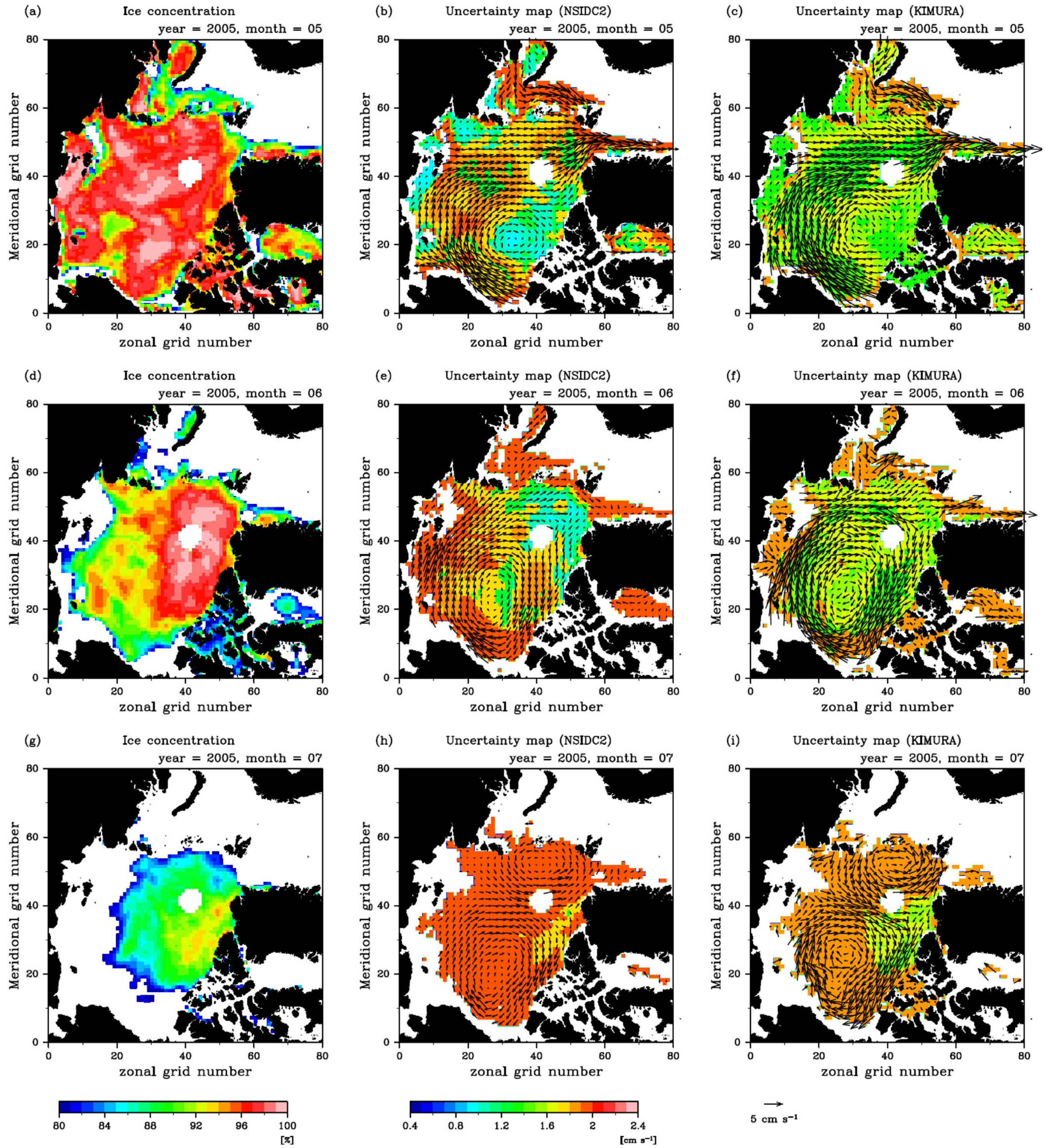

Figure 10. Monthly mean ice concentration from OSISAF (left column) and uncertainty of the monthly mean ice drift (center column: NSIDC2, right column: KIMURA) for May (top row), June (middle row), and July (bottom row) in 2005. In the left plots, ice concentration higher than 80% are shown by color. In the center and right plots, the vector fields exhibit ice drift, whereas the color indicates magnitude of the uncertainty. Note that the vector scaling of the ice drift is the same with those in Figure 4, whereas the color scale for the uncertainty differs from those in Figure 4.

range. Since both $\delta_{||\vec{U}||}$ and δ_a for NSIDC2 are more sensitive to the variation of ice drift speed and ice concentration compared to KIMURA, the empirical uncertainty function ϵ for NSIDC2 exhibits larger variation compared to that for KIMURA.

The empirical uncertainty functions are applied to the monthly mean ice drift field of both products. Figure 10 is an example of spatial maps of uncertainty from May to July 2005. The uncertainty of each ice drift vector is calculated from (8) as a function of ice drift speed and ice concentration, and mapped together with the corresponding drift vectors. The map reasonably captures the uncertainty difference between different ice drift speed areas, and the increase of uncertainty with the progress of the summer melting season.

5. Concluding Remarks

We formulated empirical uncertainty functions for monthly mean Arctic ice drift from two Eulerian products by the use of high-resolution Lagrangian ice drift obtained from SAR. The uncertainty formulation was conducted on the Eulerian basis, different from a number of previous studies done on the Lagrangian basis. In order to formulate the uncertainty function, first we deduced Eulerian ice drifts by spatial and temporal averages of the Lagrangian drifts from the RGPS data. The high spatial density of the Lagrangian drift enables us to derive monthly mean Eulerian drift with a sufficiently small estimation error. We used the estimated Eulerian drift as a references for the error assessment of the selected Eulerian products. The error of the drift was measured by the deviation from the RGPS drift, and the error was examined in relation to the drift speed and the ice concentration. The results show that the distribution functions of the errors are reasonably represented by lognormal functions in both cases. We defined the uncertainty by the 68.3 percentile of the cumulative density function of the distribution function, and combined the uncertainty for ice drift speed and ice concentration to formulate an empirical uncertainty function. The estimated uncertainty function reasonably represents the spatial and temporal variations of ice drift uncertainties, depending on drift speed and ice concentration.

Tables 1 and 2 summarize the estimated uncertainties associated with ice drift speed and ice concentration for the NSIDC2 and the KIMURA product. The values in this table indicate that the summer ice drift products are of practical use to validate model results and to constrain models by data assimilation, because the differences of the ice drift obtained from different Arctic ocean-sea ice models [*Martin and Gerdes*, 2007] are clearly larger than the uncertainty presented here. The uncertainty can be directly applied to any kind of coordinate system without considering vector rotation, since we formulated the uncertainty as a scalar variable. The only requirement for an application is that the modeled ice drift should represent a spatial scale of O(50 km), which is a typical resolution of the climate models used in the present IPCC report.

For a practical application to model validations and data assimilations, a cost function measuring model-data misfit can be defined by a squared L^2 norm of the misfit weighted by the uncertainty of the observations,

$$J=[\boldsymbol{d}-\boldsymbol{M}(\boldsymbol{m})]^T\boldsymbol{W}^{-1}[\boldsymbol{d}-\boldsymbol{M}(\boldsymbol{m})], \quad (9)$$

where $\boldsymbol{d}=[d_1,d_2,\ldots,d_N]$ is the observational data, $\boldsymbol{m}=[m_1,m_2,\ldots,m_M]$ is the control vector to be optimized (or fixed internal and external parameters for a forward model), $\boldsymbol{M}(\boldsymbol{m})=[M_1(\boldsymbol{m}),M_2(\boldsymbol{m}),\ldots,M_N(\boldsymbol{m})]$ is the model operator providing the counterparts to the observation, and $\boldsymbol{W}$ is the error covariance matrix taking the uncertainties of the observation into account. The present study gives the diagonal elements of the matrix $\boldsymbol{W}$, i.e., the i-th diagonal element (error variance) is given by

$$W_{ii}=\epsilon\left(||\vec{U}_i^{obs}||,a_i\right)^2, \quad (10)$$

where $||\vec{U}_i^{obs}||$ and a_i are the observed ice drift speed and ice concentration corresponding to the i-th drift, respectively (see equation (8)). Since the uncertainty function ϵ is formulated for the difference of vector variables, each element of the cost function should be measured by

Table 1. Uncertainty of Ice Drift Vector in Different Ice Drift Speed Range

	0 – 1 cm s^{-1}	1 – 2 cm s^{-1}	2 – 3 cm s^{-1}	3 – 4 cm s^{-1}	4 – 5 cm s^{-1}	> 6 cm s^{-1}
NSIDC2	1.0	1.1	1.8	1.8	1.3	1.8
KIMURA	1.3	1.5	1.7	1.7	1.4	1.4

Unit [cm s^{-1}]

Table 2. Uncertainty of Ice Drift Vector in Different Ice Concentration Range

	< 90%	90 – 92%	92 – 94%	94 – 96%	96 – 98%	98 – 100%
NSIDC2	2.0	1.9	1.7	1.3	1.0	0.8
KIMURA	1.8	1.5	1.6	1.4	1.3	1.2

Unit [cm s^{-1}]

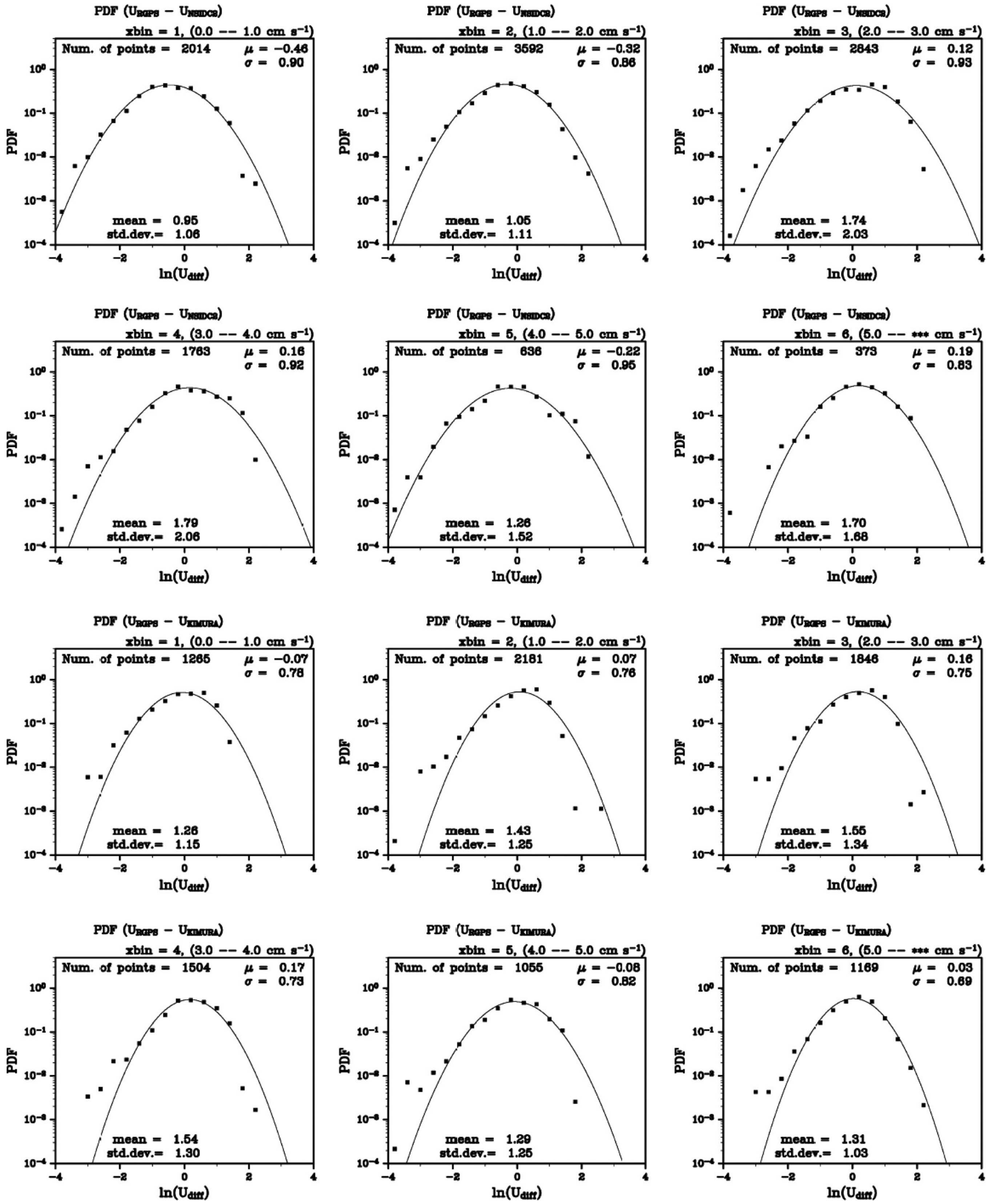

Figure A1. Probability density functions of ice drift error in respective ice drift speed bins for NSIDC2 (the first and second row) and KIMURA (the third and fourth row).

$$J_i = ||\vec{U}_i^{obs} - \vec{U}_i^{mod}|| W_{ii}^{-1}, \quad (11)$$

where $\vec{U}_i^{mod} = M_i(\boldsymbol{m})$ is the modeled ice drift corresponding to the i-th observation. It should be noted that in the present uncertainty definition we use the 68.3 percentile of the cumulative function of the lognormal distribution in place of one standard deviation of a Gaussian distribution. If one intends to deal with the error in Gaussian form, one has to evaluate the cost function by log-transformed variables.

In the present study, we have taken only the diagonal elements of the error covariance matrix into account (implicitly assuming the independence of the errors between the monthly mean grid points). Therefore the present measure may overestimate the cost to some extent, particularly due to a potential correlation of the errors in space. The large abundance and the spatial density of available ice drift from RGPS data, on the other hand, implies the possibility to assess the error covariances (nondiagonal elements of W) of the Eulerian products. But this is outside the scope of the present study and is a topic for future research.

Appendix A

Probability density functions of ice drift error in all ice drift speed bins for NSIDC2 and KIMURA are shown in Figure A1. The method to calculate the distribution and corresponding lognormal function are described in section 4.

Acknowledgments
Funding by the Helmholtz Climate Initiative REKLIM (Regional Climate Change), a joint research project of the Helmholtz Association of German research centers (HGF) is gratefully acknowledged. This work has partly been supported by the European Commission as part of the FP7 project ACCESS—Arctic Climate Change, Economy and Society (Project 265863). We also would like to express our gratitude toward the German Federal Ministry of Education and Research (BMBF) for the support of the project "RACE—Regional Atlantic Circulation and Global Change" (0F0651 D). The authors express their gratitude for all the data provider; The RGPS ice motion data available at JPL (http://rkwok.jpl.nasa.gov/radarsat/lagrangian.html) are produced with funding from NASA's MEaSUREs program. The Polar Pathfinder Daily 25 km EASE-Grid Sea Ice Motion vectors, Version 2, were provided from NSIDC (http://nsidc.org/data/nsidc-0116.html/), KIMURA ice drift data were provided by N. Kimura at the University of Tokyo, the ice concentration data were provided by OSI SAF (OSI-409: ftp://osisaf.met.no/preprocessed/ice/conc/v1/).
The GFD-DENNOU library was used to draw the figures. The authors thank the anonymous reviewer for the constructive reviews. We also thank R. Ricker for his technical assistance and M. Thoma for a fruitful discussion.

References

Colony, R., and I. Rigor (1989), Arctic Ocean Buoy Program Data Report for 1 January 1986 to 31 December 1986, *Tech. Memo. APL-UW TM 6–89*, Appl. Phys. Lab., Univ. of Wash, Seattle.
Colony, R., and A. S. Thorndike (1984), An estimate of the mean field of Arctic sea ice motion, *J. Geophys. Res.*, *89*(C6), 10,623–10,629.
Comiso, J. C. (2002) A rapidly declining perennial sea ice cover in the Arctic, *Geophys. Res. Lett.*, *29*(20), 1956, doi:10.1029/2002GL015650.
Comiso, J. C., C. L. Parkinson, R. Gersten and L. Stock (2008), Accelerated decline in the Arctic sea ice cover, *Geophys. Res. Lett.*, *35*, L01703, doi:10.1029/2007GL031972.
Dai, M., T. E. Arbetter, W. N. Meier (2006), Data assimilation of sea-ice motion vectors: Sensitivity to the parameterization of sea-ice strength, *Ann. Glaciol.*, *44*, 357–360.
Eastwood, S., K. R. Larsen, T. Lavergne, E. Nielsen, and R. Tonboe (2010), *Global Sea Ice Concentration Reprocessing Product User Manual, Product OSI-409*, The EUMETSAT Network of Satellite Appl. Facil.
Fily, M., and D. A. Rothrock (1987), Sea ice tracking by nested correlations, *IEEE Trans. Geosci. Remote Sens.*, *25*, 570–580.
Fowler, C., W. Emery, and M. Tschudi (2013), *Polar Pathfinder Daily 25 km EASE-Grid Sea Ice Motion Vectors, Version 2, (daily and mean gridded field)*, NASA DAAC at the Natl. Snow and Ice Data Cent., Boulder, Colo.
Geiger, C. A., W. D. Hibler III, and S. F. Ackley (1998), Large-scale sea ice drift and deformation: Comparison between models and observations in the western Weddell Sea during 1992, *J. Geophys. Res.*, *103*(C10), 21,893–21,913.
Geiger, C. A., Y. Zhao, A. K. Liu, and S. Häkkinen (2000), Large-scale comparison between buoy and SSM/I drift and deformation in the Eurasian Basin during winter 1992–1993, *J. Geophys. Res.*, *105*(C2), 3357–3368.
Girard-Ardhuin, F., R. Ezraty (2012), Enhanced Arctic sea ice drift estimation merging radiometer and scatterometer data, *IEEE Trans. Geosci. Remote Sens.*, *50*(7), 2639–2648, doi:10.1109/TGRS.2012.2184124.
Girard, L., J. Weiss, J. M. Molines, B. Barnier, and S. Bouillon (2009), Evaluation of high-resolution sea ice models on the basis of statistical and scaling properties of Arctic sea ice drift and deformation, *J. Geophys. Res.*, *114*, C08015, doi:10.1029/2008JC005182.
Hwang, B. (2013), Inter-comparison of satellite sea ice motion with drifting buoy data, *Int. J. Remote Sens.*, *34*(24), 8741–8763, doi:10.1080/01431161.2013.848309.
Hwang, B., and T. Lavergne (2010), *Validation and Comparison of OSI SAF Low and Medium Resolution and IFREMER/Cersat Sea Ice Drift Products, ČDOP-SG06-VS02*, The EUMETSAT Network of Satellite Appl. Facil.
Isaaks, E., and R. M. Srivastava (1989), *An Introduction to Applied Geostatistics*, Oxford Univ. Press, N. Y.
Kalnay, E., et al. (1996), The NCEP/NCAR 40-Year Reanalysis Project. *Bull. Am. Meteorol. Soc.*, *77*, 437–471.
Kimura, N., and M. Wakatsuchi (2000), Relationship between sea- ice motion and geostrophic wind in the northern hemisphere, *Geophys. Res. Lett.*, *27*(22), 3735–3738.
Kimura, N., and M. Wakatsuchi (2004), Increase and decrease of sea ice area in the Sea of Okhotsk: Ice production in coastal polynyas and dynamical thickening in convergence zones, *J. Geophys. Res.*, *109*, C09S03, doi:10.1029/2003JC002196.
Kimura, N., A. Nishimura, Y. Tanaka, and H. Yamaguchi (2013), Influence of winter sea ice motion on summer ice cover in the Arctic, *Polar Res.*, *32*, 20193, doi:10.3402/polar.v32i0.20193.
Kreyscher, M., M. Harder, P. Lemke, and G. M. Flato (2000), Results of the Sea Ice Model Intercomparison Project: Evaluation of sea ice rheology schemes for use in climate simulations, *J. Geophys. Res.*, *105*(C5), 11,299–11,320.
Kwok, R. (1998), The RADARSAT Geophysical Processor System, In *Analysis of SAR Data of the Polar Oceans*, edited by C. Tsatsoulis and R. Kwok, pp. 237–257, Springer, Berlin.
Kwok, R. (2002), Arctic sea-ice area and volume production: 1996/97 versus 1997/98, *Ann. Glaciol.*, *34*, 447–453.
Kwok, R. (2006), Contrasts in sea ice deformation and production in the Arctic seasonal and perennial ice zones, *J. Geophys. Res.*, *111*, C11S22, doi:10.1029/2005JC003246.
Kwok, R. (2008), Summer sea ice motion from the 18 GHz channel of AMSR-E and the exchange of sea ice between the Pacific and Atlantic sectors, *Geophys. Res. Lett.*, *35*, L03504, doi:10.1029/2007GL032692.
Kwok, R. (2009), Outflow of Arctic Ocean Sea Ice into the Greenland and Barents Seas: 1979–2007, *J. Clim.*, *22*, 2438–2457, doi:10.1175/2008JCLI2819.1.
Kwok, R., and G. F. Cunningham (2002), Seasonal ice area and volume production of the Arctic Ocean: November 1996 through April 1997, *J. Geophys. Res.*, *107*(C10), 8038, doi:10.1029/2000JC000469.

Kwok, R., and G. F. Cunningham (2014), *RADARSAT Geophysical Processor System Data User's Handbook*, Ver. 2.0, Jet Propul. Lab., Calif. Inst. of Technol., Pasadena.
Kwok, R., J. C. Curlander, R. McConnell, and. S. S. Pang (1990), An ice motion tracking system at the Alaska SAR facility, *IEEE J. Ocean. Eng.*, *15*, 44–54.
Kwok, R., A. Schweiger, D. A. Rothrock, S. Pang, and C. Kottmeier (1998), Sea ice motion from statellite passive microwave imagery assessed with ERS SAR and buoy motions, *J. Geophys. Res.*, *103*(C4), 8191–8214.
Kwok, R., G. F. Cunningham, and D. Nguyen (2000), *RADARSAT Geophysical Processor System Production Specification*, Ver. 2.0, Jet Propul. Lab., Calif. Inst. of Technol., Pasadena.
Kwok, R., E. C. Hunke, W. Maslowski, D. Menemenlis, and J. Zhang (2008), Variability of sea ice simulations assessed with RGPS kinematics, *J. Geophys. Res.*, *113*, C11012, doi:10.1029/2008JC004783.
Kwok, R., G. Spreen, and S. Pang (2013), Arctic sea ice circulation and drift speed: Decadal trends and ocean currents, *J. Geophys. Res. Oceans*, *118*, 2408–2425, doi:10.1002/jgrc.20191.
Lavergne, T., S. Eastwood, Z. Teffah, H. Schyberg, and L.-A. Breivik (2010), Sea ice motion from low-resolution satellite sensors: An alternative method and its validation in the Arctic, *J. Geophys. Res.*, *115*, C10032, doi:10.1029/2009JC005958.
Lindsay, R. W. (2002), Ice deformation near SHEBA, *J. Geophys. Res.*, *107*(C10), 8042, doi:10.1029/2000JC000445.
Lindsay, R. W., and H. L. Stern (2003), The RADARSAT geophysical processor system: Quality of sea ice trajectory and deformation estimates, *J. Atmos. Oceanic Technol. 20*, 1333–1347.
Lindsay, R. W., J. Zhang, A. Schweiger, M. Steele, and H. Stern (2009), Arctic sea ice retreat in 2007 follows thinning trend, *J. Clim.*, *22*, 165–176, doi:10.1175/2008JCLI2521.1.
Martin, T., and R. Gerdes (2007), Sea ice drift variability in Arctic Ocean Model Intercomparison Project models and observation, *J. Geophys. Res.*, *112*, C04S10, doi:10.1029/2006JC003617.
McPhee, M. (2008), *Air-Ice-Ocean Interaction: Turbulent Ocean Boundary Layer Exchange Processes*, Springer, Berlin.
Meier, W. N., J. A. Maslanik, and C. W. Fowler (2000), Error analysis and assimilation of remotely sensed ice motion within an Arctic sea ice model, *J. Geophys. Res.*, *105*(C2), 3339–3356.
Menke, W. (1989), Geophysical data analysis: Discrete inverse theory (revised edition), in Int. Geophys. Ser., vol. 45, edited by R. Dmowska and J. R. Holton, Academic, San Diego, Calif.
Miller, P. A., S. W. Laxon, D. L. Feltham, and D. J. Gresswell (2006), Optimization of a sea ice model using basinwide observations of Arctic Sea ice thickness, extent, and velocity, *J. Clim.*, *19*(7), 1089–1108.
Nguyen, A. T., D. Menemenlis, and R. Kwok (2011), Arctic ice-ocean simulation with optimized model parameters: Approach and assessment, *J. Geophys. Res.*, *116*, C04025, doi:10.1029/2010JC006573.
Rampal, P., J. Weiss, and D. Marsan (2009), Positive trend in the mean speed and deformation rate of Arctic sea ice, 1979–2007, *J. Geophys. Res.*, *114*, C05013, doi:10.1029/2008JC005066.
Rampal, P., J. Weiss, C. Dubois, and J.-M. Campin (2011) IPCC climate models do not capture Arctic sea ice drift acceleration: Consequences in terms of projected sea ice thinning and decline, *J. Geophys. Res.*, *116*, C00D07, doi:10.1029/2011JC007110.
Rollenhagen, K., R. Timmermann, T. Janjić, J. Schröter, and S. Danilov (2009), Assimilation of sea ice motion in a finite-element sea ice model, *J. Geophys. Res.*, *114*, C05007, doi:10.1029/2008JC005067.
Rozman, P., J. A. Hölemann, T. Krumpen, R. Gerdes, C. Köberle, T. Lavergne, S. Adams, and F. Girard-Ardhuin (2011), Validating satellite derived and modelled sea-ice drift in the Laptev Sea with in situ measurements from the winter of 2007/08, *Polar Res.*, *30*, 7218, doi: 10.3402/polar.v30i0.7218.
Sakov, P., F. Counillon, L. Bertino, K. A. Lisæter, P. R. Oke, and A. Korablev (2012), TOPAZ4: An ocean-sea ice data assimilation system for the North Atlantic and Arctic, *Ocean Sci.*, *8*, 633–656, doi:10.5194/os-8-633-2012.
Spreen, G., S. Kern, D. Stammer, and E. Hansen (2009), Fram Strait sea ice volume export estimated between 2003 and 2008 from satellite data, *Geophys. Res. Lett.*, *36*, L19502, doi:10.1029/2009GL039591.
Spreen, G., R. Kwok, and D. Menemenlis (2011), Trends in Arctic sea ice drift and role of wind forcing: 1992–2009, *Geophys. Res. Lett.*, *38*, L19501, doi:10.1029/2011GL048970.
Stark, J. D., J. Ridley, M. Martin, and A. Hines (2008), Sea ice concentration and motion assimilation in a sea ice-ocean model, *J. Geophys. Res.*, *113*, C05S91, doi:10.1029/2007JC004224.
Stern, H. L. and R. E. Moritz (2002), Sea ice kinematics and surface properties from RADARSAT synthetic aperture radar during the SHEBA drift, *J. Geophys. Res.*, *107*(C10), 8028, doi:10.1029/2000JC000472.
Sumata, H., F. Kauker, R. Gerdes, C. Köberle, and M. Karcher (2013), A comparison between gradient descent and stochastic approaches for parameter optimization of a sea ice model, *Ocean Sci.*, *9*, 609–630, doi:10.5194/os-9-609-2013.
Sumata, H., T. Lavergne, F. Girard-Ardhuin, N. Kimura, M. A. Tschudi, F. Kauker, M. Karcher, and R. Gerdes (2014), An intercomparison of Arctic ice drift products to deduce uncertainty estimates, *J. Geophys. Res. Oceans*, *119*, 4887–4921, doi:10.1002/2013JC009724.
Thorndike, A. S., and L. Colony (1982), Sea ice motion in response to geostrophic winds, *J. Geophys. Res.*, *87*(C8), 5845–5852, doi:10.1029/JC087iC08p05845.
Tremblay, L.-B., and M. Hakakian (2006), Estimating the sea ice compressive strength from satellite-derived sea ice drift and NCEP reanalysis data, *J. Phys. Oceanogr.*, *36*(11), 2165–2172.
Tschudi, M., C. Fowler, J. Maslanik, and J. Stroeve (2010), Tracking the movement and changing surface characteristics of Arctic Sea Ice, *IEEE J. Sel. Top. Appl. Earth Observ. Remote Sens.*, *3*(4), 536–540, doi:10.1109/JSTARS.2010.2048305.
Turner, J., and J. Overland (2009), Contrasting climate change in the two polar regions, *Polar Res.*, *28*(2), 146–164.
Wadhams, P. (2002), Ice in the Ocean, Gordon and Breach, London, U. K.
Wang, X., and J. Zhao (2012), Seasonal and inter-annual variations of the primary types of the Arctic sea-ice drifting patterns, *Adv. Polar Sci.*, *23*(2), 72–81, doi:10.3724/SP.J.1085.2012.00072.
Wu, B., J. Wang, and J. E. Walsh (2006), Dipole anomaly in the winter arctic atmosphere and its association with sea ice motion, *J. Clim.*, *19*, 210–225.
Zhang, J., D. R. Thomas, D. A. Rothrock, R. W. Lindsay, Y. Yu, and R. Kwok (2003), Assimilation of ice motion observations and comparisons with submarine ice thickness data, *J. Geophys. Res.*, *108*(C6), 3170, doi:10.1029/2001JC001041.